

## X-ray standing wave analysis of nanostructures using partially coherent radiation

M. K. Tiwari, Gangadhar Das, and M. J. Bedzyk

Citation: [Applied Physics Letters](#) **107**, 103104 (2015); doi: 10.1063/1.4930228

View online: <http://dx.doi.org/10.1063/1.4930228>

View Table of Contents: <http://scitation.aip.org/content/aip/journal/apl/107/10?ver=pdfcov>

Published by the [AIP Publishing](#)

---

### Articles you may be interested in

[New developments for the investigation of hard X-rays emitted by peeling adhesive tapes](#)

*Rev. Sci. Instrum.* **84**, 055104 (2013); 10.1063/1.4803155

[X-ray irradiation of soda-lime glasses studied in situ with surface plasmon resonance spectroscopy](#)

*J. Appl. Phys.* **113**, 113104 (2013); 10.1063/1.4794807

[Real time x-ray studies during nanostructure formation on silicon via low energy ion beam irradiation using ultrathin iron films](#)

*Appl. Phys. Lett.* **101**, 263104 (2012); 10.1063/1.4773202

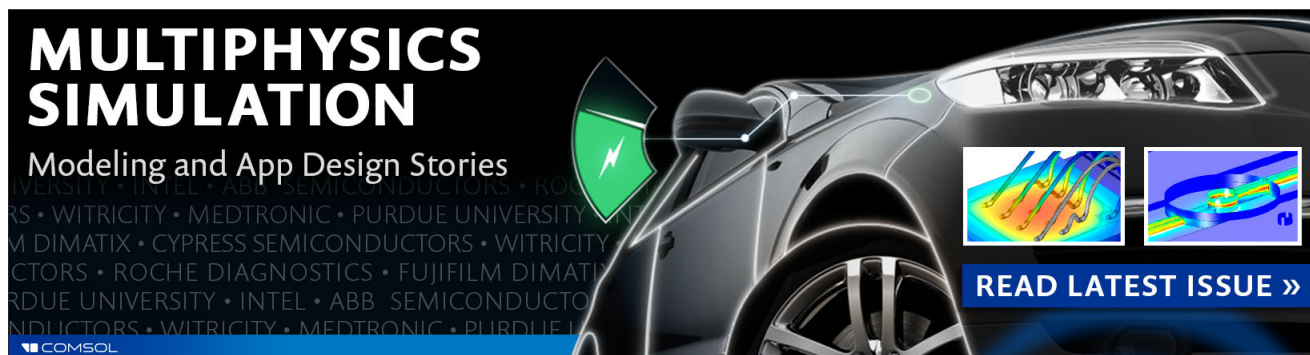
[Observations of x-ray radiation pressure force on individual gold nanocrystals](#)

*Appl. Phys. Lett.* **89**, 053121 (2006); 10.1063/1.2227713

[Surface photochemistry induced by x-ray irradiation](#)

*J. Vac. Sci. Technol. B* **16**, 3535 (1998); 10.1116/1.590491

---

The advertisement features a dark background with a sleek, modern car. On the left, the text 'MULTIPHYSICS SIMULATION' is written in large, bold, white letters. Below it, 'Modeling and App Design Stories' is written in a smaller white font. A green shield icon with a white lightning bolt is positioned to the left of the car. On the right side of the car, there are two small inset images showing simulation results: one with a color gradient and another with a blue and yellow pattern. At the bottom right, a blue button with white text says 'READ LATEST ISSUE >>'. The COMSOL logo is visible in the bottom left corner.

**MULTIPHYSICS  
SIMULATION**  
Modeling and App Design Stories

**READ LATEST ISSUE >>**

COMSOL

# X-ray standing wave analysis of nanostructures using partially coherent radiation

M. K. Tiwari,<sup>1,a)</sup> Gangadhar Das,<sup>1</sup> and M. J. Bedzyk<sup>2</sup>

<sup>1</sup>Indus Synchrotrons Utilization Division, Raja Ramanna Centre for Advanced Technology, Indore-452013, Madhya Pradesh, India

<sup>2</sup>Departments of Materials Science & Engineering and Physics & Astronomy, Northwestern University, Evanston, Illinois 60208, USA

(Received 23 July 2015; accepted 22 August 2015; published online 9 September 2015)

The effect of longitudinal (or temporal) coherence on total reflection assisted x-ray standing wave (TR-XSW) analysis of nanoscale materials is quantitatively demonstrated by showing how the XSW fringe visibility can be strongly damped by decreasing the spectral resolution of the incident x-ray beam. The correction for nonzero wavelength dispersion ( $\delta\lambda \neq 0$ ) of the incident x-ray wave field is accounted for in the model computations of TR-XSW assisted angle dependent fluorescence yields of the nanostructure coatings on x-ray mirror surfaces. Given examples include 90 nm diameter Au nanospheres deposited on a Si(100) surface and a 3 nm thick Zn layer trapped on top a 100 nm Langmuir-Blodgett film coating on a Au mirror surface. Present method opens up important applications, such as enabling XSW studies of large dimensioned nanostructures using conventional laboratory based partially coherent x-ray sources. © 2015 AIP Publishing LLC.

[<http://dx.doi.org/10.1063/1.4930228>]

Over several decades, the X-ray standing wave (XSW) technique has been developed as a nondestructive element-specific probe yielding structural analysis over length-scales ranging from 0.1 to 100 nm. The method, which is reviewed elsewhere,<sup>1–5</sup> has been widely exploited for a variety of applications including determination of positions of impurities in crystals,<sup>6–10</sup> chemically bound atoms at single crystal surfaces,<sup>11–13</sup> metallic atoms in molecular multilayer films,<sup>14</sup> ions at electrified liquid/solid interfaces,<sup>15</sup> distributions of metallic nanoparticles on surfaces,<sup>16–18</sup> as well as studies of interface structures and density variations in synthetic periodic multilayer structures.<sup>19,20</sup> In terms of x-ray wavelength  $\lambda$  and scattering angle  $2\theta$ , the probed length-scale is directly linked to the XSW period  $D = \lambda/2 \sin \theta = 2\pi/Q$ , which is 0.1–1 nm for an XSW generated by single crystal Bragg diffraction, and 8–100 nm for an XSW generated by total reflection from a mirror surface.

While understanding of the XSW technique has witnessed considerable progress, there remain a number of unexplored effects that can influence this 2-beam interference phenomenon. One such effect is the influence of the coherence properties of the incoming x-ray wave field on the XSW field intensity distribution above a reflector surface. In conventional XSW analysis, the incident wave field is assumed perfectly monochromatic plane-wave with zero wavelength dispersion ( $\delta\lambda = 0$ ), hence assuming an infinite longitudinal coherence length of the incoming x-rays. As previously demonstrated,<sup>21</sup> this simplifying assumption has no significant effect on the analysis until the optical path length difference ( $\Delta = n2z \sin \theta$ ) between the two interfering waves is significantly smaller than the longitudinal coherence length ( $L_L \approx \lambda^2/\delta\lambda$ ), where  $n$  is the index of refraction,  $z$  is the height of the probed atomic layer above the mirror

surface, and  $\delta\lambda$  is the FWHM of the spectral distribution. Beyond this constraint, XSW analysis will not match well to measurements, if the longitudinal coherence properties of the incoming x-ray field are not properly taken into account in the model calculations.

Herein, we extend the analysis method beyond the zero-bandwidth approximation to include the influence of longitudinal coherence properties of the incoming x-ray field on XSW measurements. We will show that the derived numerical solutions developed to account for the coherence properties of a source can be directly adapted in the computation of the angle-dependent XSW field pattern produced by a partially coherent x-ray beam, characterized with a Gaussian distribution in intensity and a finite spectral bandwidth. This approach allows us to perform XSW analysis with improved reliability using most x-ray sources currently available, which offer finite spectral resolutions for the incoming x-rays. To explicitly demonstrate the applicability of our modified XSW approach, we performed XSW analysis on several nanostructured materials, deposited on Si or Au mirror surfaces using different incident x-ray beams with different longitudinal coherence properties.

It is convenient to express the electric field intensity at height  $z$  above a reflecting surface (Fig. 1) by<sup>22</sup>

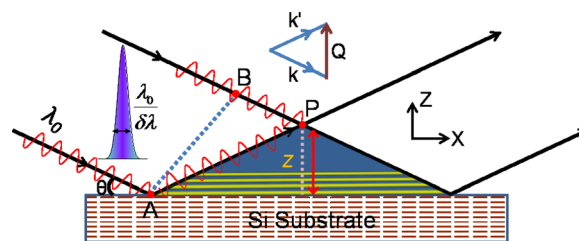


FIG. 1. A schematic illustration describing formation of XSW field under total external reflection of x-rays on a mirror surface.

<sup>a)</sup>mktiwari@rrcat.gov.in

$$I(\theta, z) = |\mathbf{E}_o^i + \mathbf{E}_o^r|^2 = I_o \{1 + R + 2\sqrt{R} \times \text{Re}[\gamma(\Delta)]\}, \quad (1)$$

where  $R = |E_o^r/E_o^i|^2$  represents the reflectivity above the Si mirror surface,  $I_o = |E_o^i|^2$  is the incident intensity,  $\mathbf{E}_o^i$  and  $\mathbf{E}_o^r$ , respectively, describe amplitudes of the incident and reflected x-ray wave fields, the complex degree of coherence  $\gamma(\Delta) = |\gamma_{ir}(\Delta)| \times \exp(i[\nu(\theta) - Q_z z])$  accounts for the interference between the incident and reflected wave fields,  $Q_z = 4\pi \sin \theta / \lambda$  represents  $z$ -component of scattering vector  $\vec{Q} = \vec{k}^i - \vec{k}^r$ ,  $\nu(\theta)$  is the phase of the E-field amplitude ratio and  $\theta$  is the glancing incidence angle on the mirror surface. In the above expression, we have introduced an additional term  $|\gamma_{ir}(\Delta)|$  that signifies the modulus of the degree of mutual coherence<sup>23,24</sup> between incident and reflected x-ray waves above the mirror surface. Its value changes from 0 to 1 and strongly depends on the optical path length difference  $\Delta = n(AP - BP) \approx n2z \sin \theta$  between two wave fields.

Fig. 2(a) depicts simulation for the term  $\text{Re}[\gamma(\Delta)]$  as a function of path length difference, (represented in terms of height  $z$ ) above the substrate surface at incidence angle of  $\theta \approx 0.114^\circ$ . While Figure 2(b) shows contour plot for the x-ray field intensity distribution computed as a function of height  $z$  and incidence angle  $\theta$  on top of the Si substrate surface. In the contour plot (Fig. 2(b)), one clearly observes a boundary for the critical angle of the Si substrate. The visibility contrast of XSW interference fringes is significantly higher below the critical angle  $\theta_c \approx 0.114^\circ$ . The results presented in Figures 2(a) and 2(b) have been simulated for incident x-rays of 15 keV and considering a spectral resolution of  $\lambda_o/\delta\lambda \approx 5000$ , described by a Gaussian distribution profile  $I(\lambda) = \frac{I_o}{\sqrt{2\pi}(\delta\lambda/2.35)} \exp[-\frac{(\lambda-\lambda_o)^2}{2(\delta\lambda/2.35)^2}]$  as shown in the inset of Fig. 2(a). It can be further observed from Fig. 2(a), at a large value of spectral resolution, the amplitude of real part  $\gamma(\Delta)$

remains unchanged up to the height  $z = 300$  nm above the substrate surface. This is because at this incident angle the optical path length difference between the incident and reflected waves at  $z = 300$  nm is  $\Delta \sim 1.2$  nm, which is much smaller than the longitudinal coherence length (413 nm).

Figures 2(c) and 2(d), respectively, report simulations obtained for the incident x-rays energy of 15 keV comprising a spectral resolution of  $\lambda_o/\delta\lambda \approx 6.22$ . From Fig. 2(c), it can be seen that at large height above the substrate surface, for example, at  $z \geq 150$  nm, the incident and reflected beams hardly remain coherent with each other. As a result, the interference term in Eq. (1) vanishes, and the total x-ray intensity above the substrate simply represents the sum of the intensity of the incident and reflected x-rays beams (refer to Fig. 2(d)). Furthermore, it can also be noticed from Fig. 2(d) that the XSW interference modulations below critical angle are strongly correlated with  $\gamma(\Delta)$  value. If path length difference  $\Delta$  (for a given height  $z$ ), between two interfering beams, is significantly smaller than the coherence length (i.e.,  $\Delta \ll L_L$ ), then a XSW with high fringe visibility,  $V = (I_{max} - I_{min})/(I_{max} + I_{min})$ , is produced in the total reflection region. As the path length ( $\Delta$ ) is increased, the XSW fringe visibility is reduced. For example, for incident x-rays of energy  $\sim 15$  keV comprising of spectral resolution of  $\lambda_o/\delta\lambda \approx 6.22$ , the coherence length  $L_L \approx 0.51$  nm (FWHM), which corresponds to a path length value  $z \approx 129$  nm above the substrate surface. At this height, the visibility of the XSW fringe reduced to  $\sim 50\%$ . For large heights ( $z \gg L_L$ ), the interference effect completely vanishes and the net intensity below the critical angle attains maximum value  $\approx 2I_o$ .

Next, we demonstrate the applicability of our methodology by, analyzing a few nanostructured materials using a well-characterized partial coherent x-ray radiation.

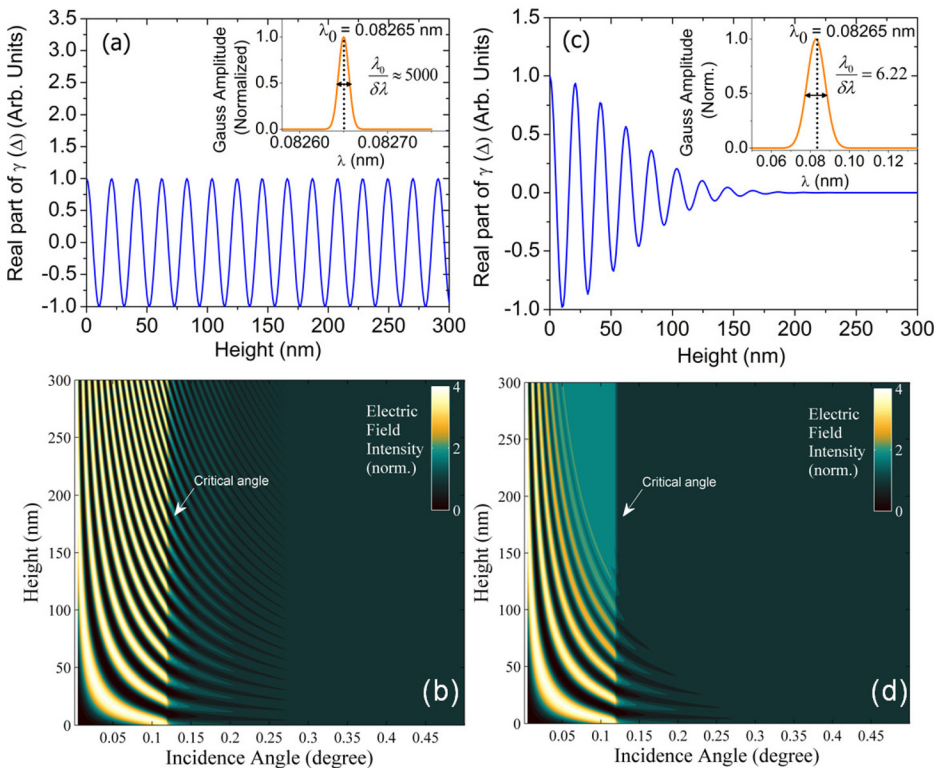


FIG. 2. Variation of  $\text{Re}[\gamma(\Delta)]$  and computed x-ray field intensity distribution above the Si substrate surface for the 15 keV x-rays at two different spectral resolutions. (a) and (b) show simulation results obtained at spectral resolution of  $\lambda_o/\delta\lambda \approx 5000$ . While (c) and (d) depict simulation results obtained at low spectral resolution of  $\lambda_o/\delta\lambda \approx 6.22$ . (a) and (c) are calculated at the critical angle  $\theta_c \approx 0.114^\circ$ .

*Au nanoparticle distribution on Si (100) surface*—Figure 3(a) depicts simulation results for the Au nanoparticles distribution on the Si(100) surface, which clearly reveal deeper insights on how monochromaticity of the partially coherent x-ray radiation affects the sensitivity of the total reflection assisted x-ray standing wave (TR-XSW) assisted angle dependent Au-L $\alpha$  fluorescence yield of the Au nanoparticles. The TR-XSW assisted Au-L $\alpha$  fluorescence profiles were computed at different spectral widths of the incident x-ray radiation assuming spherical shape of the Au nanoparticles (dia.  $\approx$  250 nm). It can be noted from Fig. 3(a) that the XSW assisted Au-L $\alpha$  fluorescence profile of the nanoparticles undergoes slowly with a distinct and systematic variation as we allow to vary monochromaticity of the incident x-ray radiation ( $\lambda_0/\delta\lambda = \infty$  to 6.22). The visibility contrast of the XSW induced Au-L $\alpha$  fluorescence oscillations decreases gradually in the total reflection region ( $\theta < 0.114^\circ$ ) at the lower spectral resolutions. Even, many XSW oscillations vanish completely in the computed Au-L $\alpha$  fluorescence profile at spectral resolution  $\lambda_0/\delta\lambda \approx 6.22$ , which can be

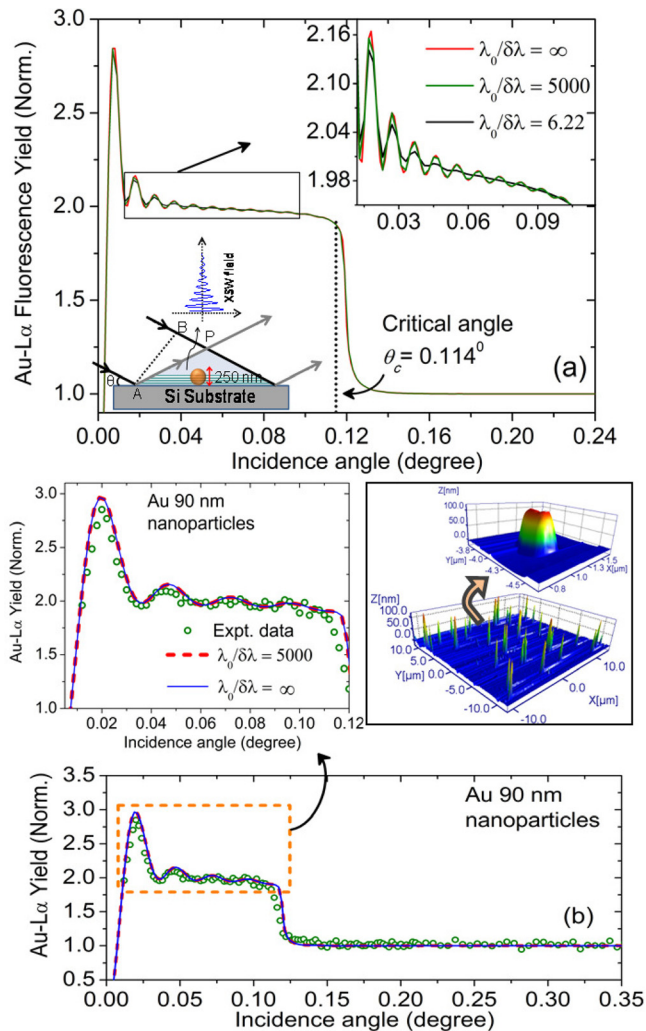


FIG. 3. (a) Computed XSW induced fluorescence profiles for spherical Au nanoparticles distribution on a Si substrate using Eq. (1) and the formula presented by von Bohlen *et al.*<sup>18</sup> at different spectral resolution widths of the incoming x-ray beam. (b) Comparison of measured to calculated Au fluorescence yields. AFM image of Au nanoparticles distribution on Si surface is shown in upper right along with enlarged image of a single nanoparticle.

clearly seen from the expanded view as shown in the inset of Fig. 3(a).

The experimental measurements for the Au nanoparticles distribution comprising of an average particle size  $D \sim 90$  nm (dia.), dispersed on a Si(100) substrate surface were carried out at the BL-16 beamline of Indus-2 synchrotron radiation facility.<sup>25</sup> Incident x-rays of energy 15 keV from bending magnet source, monochromatized with a fixed exit Si (111) double-crystal monochromator was used to excite nanoparticle samples at grazing incidence angles. Au-L $\alpha$  fluorescence x-rays emitted from the gold nanoparticles were collected by a Vortex spectroscopy detector. Figure 3(b) depicts experimentally measured XSW induced Au-L $\alpha$  fluorescence profile for the Au nanoparticles along with the computed TR-XSW profiles at different spectral resolutions. The counting statistics of Au-L $\alpha$  intensity was ensured in the range of (1–3)%. In the computation, we have considered a polydispersity factor ( $\sigma/N_{av}$ )  $\approx$  0.05 for the Au nanoparticles, where  $N_{av}$  is the average particle size and  $\sigma$  is the r. m. s. variation in particle size. In Fig. 3(b), one observes a couple of interference oscillations in the measured XSW induced Au-L $\alpha$  fluorescence profile below the critical angle of the Si substrate ( $\theta_c \approx 0.114^\circ$ ). These peaking interference oscillations in the fluorescence profile emerge due to the coincidence of the XSW antinodes within the volume of the Au nanoparticles. The left side inset of Fig. 3(b) shows an expanded view for the total external reflection region. It can be seen that the computed fluorescence profile at spectral resolution  $\lambda_0/\delta\lambda \approx 5000$  closely agrees with the profile that obtained assuming an ideal monochromatic x-ray source (i.e.,  $\lambda_0/\delta\lambda = \infty$ ). This is due to the fact that at higher spectral resolutions, the incident and reflected x-ray beams remain fully coherent up to a height of several hundred of nanometers above the substrate surface. If the size of the nanostructure is considerably smaller than the coherence length, for example, in our case of 90 nm Au nanoparticles, then full volume of a nanostructure is excited by the XSW field created with a 100% coherent superposition of the incident and reflected x-ray beams. In conditions, if spectral resolution of the incident x-rays deteriorates or if the height of a nanostructure increases on top of the substrate surface, the measured fluorescence profile will show deviation from the ideal behavior ( $\lambda_0/\delta\lambda = \infty$ ). On the top right inset of Fig. 3(b), we have shown measured AFM image for the Au nanoparticles, which clearly demonstrates a mono-dispersed surface topography for the Au nanoparticles distribution on the Si Substrate surface.

*Langmuir-Blodgett (LB) thin film*—To demonstrate the effect of longitudinal coherence in the case of structural characterization of thin layered materials, we have performed TR-XSW analysis of a LB thin film structure deposited on top of a Au mirror surface using 10 keV incident x-rays of different spectral resolutions. This experiment used the hard-bend radiation from the D-line at the Cornell High Energy Synchrotron Source. Figs. 4(a)–4(c) show measured Zn-K $\alpha$  fluorescence profiles originated from the trapped Zn atomic layer (thickness  $\approx$  3.0 nm) at a height  $z \sim 93.3$  nm in the LB film structure using incident x-ray beam with differing longitudinal coherence lengths and a fixed angular divergence  $\approx 0.003^\circ$ . Fig. 4(a) shows Zn-K $\alpha$  fluorescence profile measured using a nearly ideal plane wave condition of

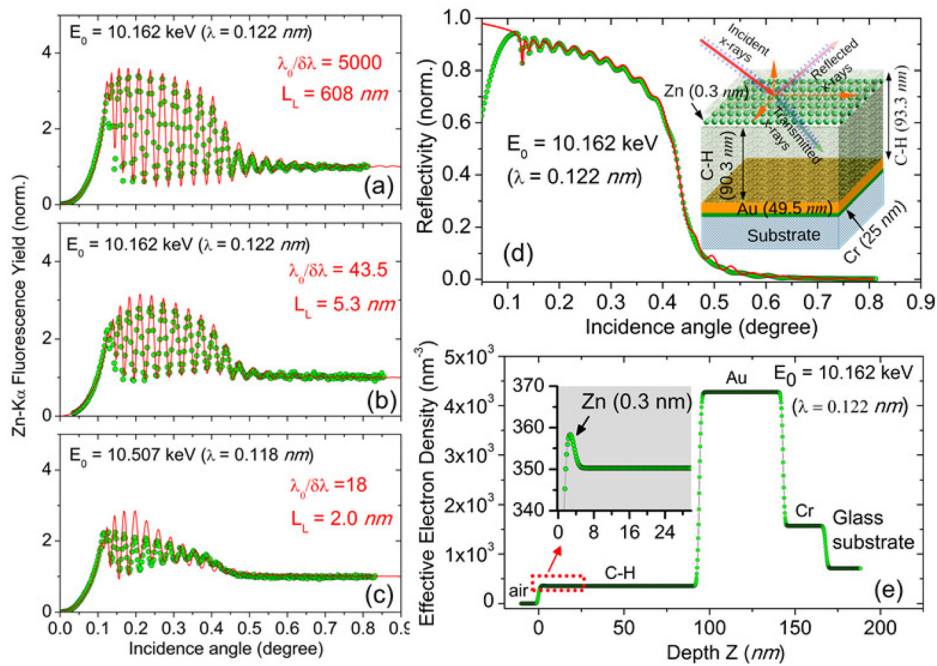


FIG. 4. Experimental demonstration of the applicability of the partially coherent radiation for TR-XSW analysis. (a)–(c) Measured and fitted angle-dependent x-ray fluorescence profiles for the Zn atomic layer embedded in a LB film structure at different spectral widths of the incident x-ray photons. The relative uncertainty in the Zn yield is less than 5% for data above  $0.45^\circ$  and less than 2% below  $0.45^\circ$ . (d) Measured and fitted x-ray reflectivity profiles for the LB thin film structure at x-ray energy of 10.162 keV with spectral resolution of  $\lambda_0/\delta\lambda \approx 5000$  corresponding to (a). (e) Effective electron density profile of the LB thin film structure determined from the best fit results using combined XRR and TR-XSW analysis, which clearly reveals the presence of Zn atomic layer at a mean height  $\langle z \rangle = 90.3$  nm, from Au surface layer.

spectral width  $\lambda_0/\delta\lambda \approx 5000$ , ( $L_L \approx 608$  nm) obtained by a Si(111) monochromator. While Figs. 4(b) and 4(c) demonstrate measured Zn-K $\alpha$  fluorescence profiles obtained using relatively wider band-pass incident x-ray beams produced by synthetic Bragg multilayer monochromators, providing spectral resolutions of  $\lambda_0/\delta\lambda \approx 43.5$  and  $\lambda_0/\delta\lambda \approx 18$ , respectively, which were determined by using the measured angular width of the reflectivity curves from two different  $hkl$  planes of a Si analyzer crystal in the sample position. The details about preparation of LB thin film structure and experimental conditions used for the measurements described in Fig. 4 are given elsewhere.<sup>14,21,26</sup> As can be seen from Figs. 4(a)–4(c), the visibility of the XSW induced oscillations in the Zn-K $\alpha$  fluorescence profile reduces dramatically as the monochromaticity ( $\lambda_0/\delta\lambda$ ) of the incident x-ray photons vary from 5000 to 18. The theoretically computed curves shown by red solid lines closely predict the experimental observations even in the cases when spectral resolution of the incident x-ray photons changed by large magnitudes ( $\approx 200$  times). This encouraging level of agreement between the experimental and computed TR-XSW profiles convinces the validity of our modified XSW approach. In Fig. 4(d), we have shown measured and fitted x-ray reflectivity (XRR) profiles obtained for the LB thin film structure at incident x-ray photon energy of 10.162 keV at highest spectral resolution corresponding to Fig. 4(a). In this figure, we have also shown a schematic layout for the LB thin film structure. Fig. 4(e) shows effective electron density profile (EDP) for the LB thin film structure determined from combined XRR and TR-XSW analysis using the best fit results obtained in all three cases. The EDP clearly reveals the presence of Zn atomic layer at location  $z \approx 90.3$  nm, from the Au layer surface.

In conclusion, we have shown that longitudinal coherence properties of a partially coherent x-ray source have an ability to efficiently modulate the XSW field intensity pattern under total reflection condition on a mirror surface. We have implemented the source properties such as spectral resolution and

its intensity distribution to account for longitudinal coherence in the model computation of fluorescence-induced XSW profile of a nanostructured material. This is in contrast to the conventional approach where the XSW analysis is performed assuming a perfectly monochromatic x-ray plane-wave incident beam. There are two technical outcomes from this finding that connects the TR-XSW fringe visibility to coherence. (1) The spectral resolution of the upstream monochromator can be designed to maximize the incident intensity and therefore fluorescence sensitivity from an atomic layer without significantly compromising the spatial resolution of the measured atomic height distribution profile. For example, certain TR-XSW measurements can be performed on a conventional X-ray tube or rotating anode source using wide-band-pass multilayer optics. (2) The TR-XSW measurement can be designed to measure the longitudinal (or temporal) coherence properties of the incident beam.

The authors would like to thank Professor Donald Bilderback, Cornell High Energy Synchrotron Source, USA, for fruitful discussions and suggestions. The data in Fig. 4 were collected at the D-Line station of the Cornell High Energy Synchrotron Source (CHESS), which is supported by the U.S. National Science Foundation. Gangadhar Das, acknowledges Homi Bhabha National Institute, India for providing research fellowship.

<sup>1</sup>J. Zegenhagen, *Surf. Sci. Rep.* **18**, 202 (1993).

<sup>2</sup>I. A. Vartanyants and M. V. Kovalchuk, *Rep. Prog. Phys.* **64**, 1009 (2001).

<sup>3</sup>M. J. Bedzyk and L. W. Cheng, *Rev. Mineral. Geochem.* **49**, 221 (2002).

<sup>4</sup>D. P. Woodruff, *Rep. Prog. Phys.* **68**, 743 (2005).

<sup>5</sup>*The X-Ray Standing Wave Technique: Principles and Applications*, edited by J. Zegenhagen and A. Kazimirov (World Scientific Publishing Co., Singapore, 2013).

<sup>6</sup>B. W. Batterman, *Phys. Rev. A* **133**, A759 (1964).

<sup>7</sup>J. A. Golovchenko, B. W. Batterman, and W. L. Brown, *Phys. Rev. B* **10**, 4239 (1974).

<sup>8</sup>L. Cheng, P. Fenter, M. J. Bedzyk, and N. C. Sturchio, *Phys. Rev. Lett.* **90**, 255503 (2003).

- <sup>9</sup>J. A. Van Bokhoven, T. L. Lee, M. Drakopoulos, C. Lamberti, S. Thiess, and J. Zegenhagen, *Nat. Mater.* **7**, 551 (2008).
- <sup>10</sup>T. L. Lee, C. Bihler, W. Schoch, W. Limmer, J. Daeubler, S. Thiess, M. S. Brandt, and J. Zegenhagen, *Phys. Rev. B* **81**, 235207 (2010).
- <sup>11</sup>J. A. Golovchenko, J. R. Patel, D. R. Kaplan, P. L. Cowan, and M. J. Bedzyk, *Phys. Rev. Lett.* **49**, 560 (1982).
- <sup>12</sup>Y. L. Qian, N. C. Sturchio, R. P. Chiarello, P. F. Lyman, T. L. Lee, and M. J. Bedzyk, *Science* **265**, 1555 (1994).
- <sup>13</sup>J. D. Emery, B. Detlefs, H. J. Karmel, L. O. Nyakiti, D. K. Gaskill, M. C. Hersam, J. Zegenhagen, and M. J. Bedzyk, *Phys. Rev. Lett.* **111**, 215501 (2013).
- <sup>14</sup>M. J. Bedzyk, G. M. Bommarito, and J. S. Schildkraut, *Phys. Rev. Lett.* **62**, 1376 (1989).
- <sup>15</sup>M. J. Bedzyk, D. H. Bilderback, G. M. Bommarito, M. Caffrey, and J. S. Schildkraut, *Science* **241**, 1788 (1988).
- <sup>16</sup>M. K. Tiwari, G. M. Bhalerao, M. Babu, A. K. Sinha, and C. Mukherjee, *J. Appl. Phys.* **103**, 054311 (2008).
- <sup>17</sup>M. K. Tiwari, K. J. S. Sawhney, T.-L. Lee, S. G. Alcock, and G. S. Lodha, *Phys. Rev. B* **80**, 035434 (2009).
- <sup>18</sup>A. von Bohlen, M. Krämer, C. Sternemann, and M. Paulus, *J. Anal. At. Spectrom.* **24**, 792–800 (2009); A. von Bohlen, M. Brücher, B. Holland, R. Wagner, and R. Hergenröder, *Spectrochim. Acta, Part B* **65**, 409–414 (2010).
- <sup>19</sup>T. Kawamura and H. Takenaka, *J. Appl. Phys.* **75**, 3806 (1994); V. Kohli, M. J. Bedzyk, and P. Fenter, *Phys. Rev. B* **81**, 054112 (2010).
- <sup>20</sup>T. Matsushita, A. Iida, T. Ishikawa, T. Nakagiri, and K. Sakai, *Nucl. Instrum. Methods Phys. Res. A* **246**, 751 (1986).
- <sup>21</sup>M. J. Bedzyk, e-print [arXiv:0908.2115](https://arxiv.org/abs/0908.2115) [cond-mat.mtrl-sci]; *The X-Ray Standing Wave Technique: Principles and Applications*, edited by J. Zegenhagen and A. Kazimirov (World Scientific, Singapore, 2013), Chap. 5.
- <sup>22</sup>D. K. G. de Boer, *Phys. Rev. B* **44**, 498 (1991).
- <sup>23</sup>M. Born and E. Wolf, *Principles of Optics*, 7th ed. (Cambridge University Press, United Kingdom, 1999), pp. 554–630.
- <sup>24</sup>M. K. Tiwari and G. Das, e-print [arXiv:1406.3581v1](https://arxiv.org/abs/1406.3581v1) [cond-mat.mes-hall].
- <sup>25</sup>M. K. Tiwari, P. Gupta, A. K. Sinha, S. R. Kane, A. K. Singh, S. R. Garg, C. K. Garg, G. S. Lodha, and S. K. Deb, *J. Synchrotron Radiat.* **20**, 386 (2013).
- <sup>26</sup>J. Wang, M. J. Bedzyk, T. L. Penner, and M. Caffrey, *Nature* **354**, 377 (1991).